Modeling Frequency Independent Hysteresis Effects of Ferrite Core Materials Using Permeance–Capacitance Analogy for System-Level Circuit Simulations

Min Luo, *Member, IEEE*, Drazen Dujic, *Senior Member, IEEE*, and Jost Allmeling, *Member, IEEE*

***Abstract*—Ferrite materials are widely used for magnetic cores in power electronic converters. The hysteresis effect of the material leads to power loss and harmonic distortion. In order to predict the behavior of the magnetic component in the system environment during the design phase, accurate system-level time-domain simulation is desired. This paper proposes an approach to model the frequency-independent magnetic hysteresis effect of ferrite core materials in magnetic circuits based on the permeance–capacitance analogy. The model is able to accurately reproduce the per-cycle energy loss and equivalent permeability of the hysteresis loops under excitation in a wide range of amplitudes.**

***Index Terms*—Ferrite material, hysteresis, magnetic circuit, permeance capacitance.**

NOMENCLATURE

B	Flux density.
B_r	Remanent flux density.
H	Field strength.
Φ	Magnetic flux.
$\mathscr{P}$	Magnetic permeance.
μ	Magnetic permeability.

I. INTRODUCTION

FERRITE materials are widely used to produce magnetic cores for inductive filters and isolation transformers in power electronic converters. In comparison to the ferromagnetic materials, such as amorphous alloy and nanocrystalline, ferrite materials have significantly lower conductivity, so that the frequency-independent magnetic hysteresis effect usually dominates the core loss. Due to the fact that the magnetic hysteresis contributes to the nonlinearity of the magnetic component's inductivity, which interacts with the remaining part of the power electronic system, the hysteresis loss is essentially a coupled effect. In order to predict the behavior of the magnetic component during design phase, an accurate time-domain hysteresis model that can be easily integrated into the system-level circuit environment and simulated in a fully coupled way is desired.

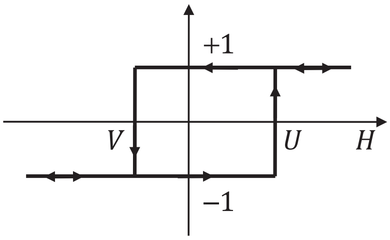

Fig. 1. Single hysteron $\gamma(U, V)$ of the Preisach model.

The permeance–capacitance analogy approach, which was proposed in [1], provides a practical way to combine magnetic circuit seamlessly into system-level simulation. The benefit in modeling complex magnetic structures using permeance–capacitor approach has been demonstrated by Yan and Lehman [2], and Allmeling *et al.* [3] have introduced this approach into a commercial system-level simulation tool for power electronics. Further on, this approach has been applied in [4] and [5] to capture different magnetic phenomena. In this paper, we also choose the permeance–capacitor approach as a fundamental platform for the modeling.

For time-domain simulation of frequency-independent magnetic hysteresis, Preisach model has been recognized as a flexible approach, especially regarding its ability to capture minor loops [6]. According to the formulation of the scalar Preisach model, the magnetic hysteresis is subdivided into many small independent particles [7], called hysterons. Each square-loop hysteron $\gamma(U, V)$ switches between -1 and $+1$ at a unique set of transition boundaries U and V, depending on the applied field strength H as well as its history, as demonstrated in Fig. 1. The flux density B is expressed as the weighted summation of all hysterons using a probability distribution function (PDF) $p(U, V)$, or in other words, Everett integration. In the case of soft-magnetic materials, such as ferrite, the two-dimensional distribution function $p(U, V)$ can be expressed as the product of two one-dimensional PDFs, considering the fact that the

---

Manuscript received November 30, 2017; accepted February 7, 2018. Date of publication February 27, 2018; date of current version September 28, 2018. This paper was supported in the frame of the ECPE Joint Research Programme. Recommended for publication by Associate Editor M. Duffy. *(Corresponding author: Min Luo.)*

M. Luo and D. Dujic are with the Power Electronics Laboratory, École Polytechnique Fédérale de Lausanne, Lausanne CH-1015, Switzerland (e-mail: min.luo@epfl.ch; drazen.dujic@epfl.ch).

J. Allmeling is with the Plexim GmbH, Zürich CH-8005, Switzerland (e-mail: allmeling@plexim.com).

Color versions of one or more of the figures in this paper are available online at http://ieeexplore.ieee.org.

Digital Object Identifier 10.1109/TPEL.2018.2809704

probability of a hysteron switching in one direction is essentially independent of that switching in the opposite direction [8]

$$B = \iint p(U,V) \cdot \gamma(U,V) \cdot dUdV$$
$$= \iint p_s(U) \cdot p_s(-V) \cdot \gamma(U,V) \cdot dUdV. \quad (1)$$

Bertotti *et al.* [9] proposed Cauchy–Lorentz PDF for the distribution function p_s, which was further applied by [10], [11], and [12] for modeling of soft-magnetic materials. A parameter identification scheme using genetic algorithm has been presented in [13]. Taking advantage of the feature that the Cauchy–Lorentz PDF has closed-form integral, the differential permeability $\mu = dB/dH$ can be analytically calculated, so that the Preisach model was able to be directly applied to the permeance–capacitor magnetic circuit model in [3]. In the existing publications, verification of the Preisach model with the Cauchy–Lorentz PDF has only been carried out on metal-based material, such as silicon steel. For ferrite, however, the Cauchy–Lorentz PDF will result in considerable error on both equivalent permeability and per-cycle energy loss, which will be discussed in a later section of this paper. To improve the accuracy, other PDFs could be adopted.

In [14], Cardelli *et al.* have developed an approach to numerically construct the PDF using experimentally measured symmetrical hysteresis loops, after discretizing $p(U,V)$ with homogeneous grids on the (U,V) plane, and assuming that inside each grid, $p(U,V)$ is constant. This approach is potentially able to capture the hysteresis of arbitrary materials including ferrites, but significant numerical error could be involved in practice, as has been discussed and improved in [15]. In order to achieve an acceptable resolution, a large number of hysteresis loops should be measured, which is in some cases impractical from engineering point of view. Consolo *et al.* [16] have introduced a discrimination function in order to reduce the number of loops necessarily to be measured. Nevertheless, calculating the Everett integration of the discretized form of $p(U,V)$ in the Preisach model could be too complicated and inefficient during time-domain simulation.

The research works in [17], [18], and [19] have explored that all the magnetization curve of the Preisach model following the formulation in (1) can be derived from the descending curve of only one measured limiting hysteresis loop (with the highest amplitude of concern), without the need of analytically identifying the PDF. Making use of this feature, symmetrical hysteresis loops with relatively large amplitude (larger than 50% of the limiting loop) have been modeled with good accuracy in [20], [21], and [22] for ferrite materials. Hysteresis loops with low amplitudes (e.g., 20% of the limiting loop), however, were not explicitly verified and no handling was specifically described to control the accuracy there. With desire to use the Preisach model for arbitrary operating conditions, the accuracy control of minor hysteresis loops requires further improvement.

It has been discussed in [23] that reversible magnetization is also present in soft-magnetic materials that cannot be captured by the classical Preisach model. Therefore, the hysteresis model should be composed of an irreversible component using the classical Preisach model and a reversible component. The reversible component is essentially a single-lined $B - H$ characteristic, for which the inverse trigonometric ($\arctan$) function proposed by Perez-Rojas [24] and hyperbolic cotangen ($\coth$) function by Jiles and Atherton [25], [26] have been adopted by Luo *et al.* [12] and Hsu and Ngo [22], respectively. This paper will still follow this methodology but a new fitting function is chosen for the reversible component, which provides an additional degrees of freedom, so that the equivalent permeability can be better controlled.

Aiming to improve the accuracy of simulating the hysteresis effect of ferrite materials in system-level time-domain simulation, this paper combines the following aspects together, by which it is distinguished from the other previous publications.

1) A logistic PDF is adopted for the irreversible component modeled by the classical Preisach model, which is able to better approximate the per-cycle hysteresis energy loss of ferrite materials. The comparison to the Cauchy-Lorentz PDF is provided in a later section.
2) An improved parameterization process is introduced for the irreversible component to control the accuracy of the per-cycle energy loss for both symmetrical large limiting- and small minor loops.
3) A new form of reversible magnetization curve is proposed, which gets the equivalent permeability of hysteresis loop at wide amplitude range under control.
4) The improved modeling's approach is seamlessly incorporated into permeance–capacitor based magnetic circuit for system level simulations.

This paper is organized as follows. Section II provides the implementation details of the classical Preisach model in permeance–capacitor magnetic circuit, as an elaboration of the corresponding part from [3]. Section III demonstrates the proposed approach of modeling together with the procedure for parameter identification. Afterward in Section IV, the fidelity of the model in simulating different ferrite materials is evaluated on a magnetic characterization setup, together with the comparison to the Preisach model using the Cauchy–Lorentz PDF. Further, in Section V, the performance of the model in simulation environment for power electronic circuits is demonstrated and evaluated.

II. CLASSICAL PREISACH MODEL

In this section, the basic concept of permeance–capacitor based magnetic circuit as well as its realization of the classical Preisach model for magnetic hysteresis is elaborated, as an extension of the corresponding part presented in [3]. The integrated magnetic structure depicted in Fig. 2(a) is taken as an example, which is composed of two E-shape cores and four electrical windings. The magnetic structure resembling the real geometry can be intuitively translated into a permeance magnetic circuit, shown in Fig. 2(b). The interface components connecting electric and magnetic circuit represent the windings (highlighted by the light blue frame), which are realized as gyrator form shown in Fig. 2(c). Each permeance block stands for a certain part of

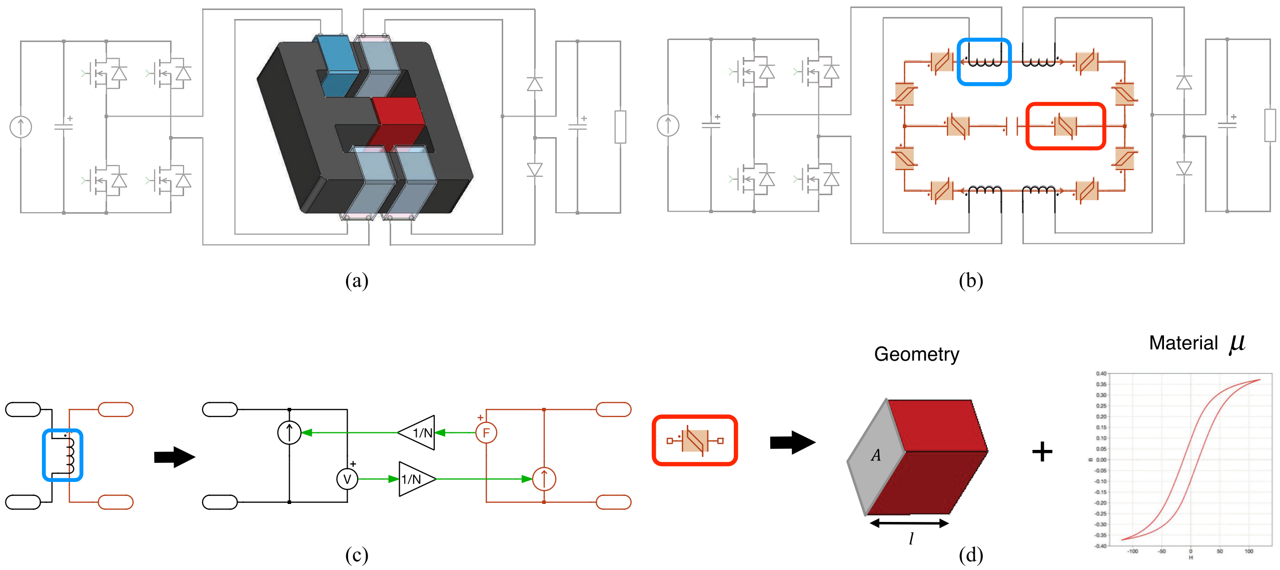

(a) (b) (c) (d)

Fig. 2. Permeance–capacitor approach. (a) Integrated magnetic component. (b) Magnetic circuit of the integrated magnetic component. (c) Winding component using gyrator structure as an interface between electrical and magnetic circuit. (d) Core block parameterized by the geometry and material characteristic.

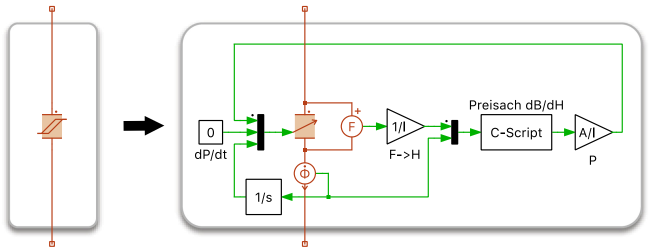

Fig. 3. Structure of the permeance block with hysteresis behavior using the classical Preisach model.

the magnetic core [e.g., the one highlighted by the red frame in Fig. 2(b) represents one-half of the middle limb in Fig. 2(a)]. In the magnetic circuit, we have the combination of the through variable (the derivative of the magnetic flux $\dot{\Phi}$) and the across variable (magnetomotive force F). The relation between $\dot{\Phi}$ and F on a single permeance block is governed by

$$\dot{\Phi} = \mathscr{P} \cdot \frac{dF}{dt}. \tag{2}$$

The permeance value P in the above-mentioned equation is calculated using the geometry and material characteristic

$$\mathscr{P} = \mu \cdot \frac{A}{l} \tag{3}$$

where A is the cross-sectional area and l is the magnetic path length. The $B-H$ characteristic of the material is reflected by the permeability μ, as illustrated in Fig. 2(d). Should the nonlinearity of material (e.g., magnetic hysteresis) be considered, μ becomes a variable depending on the field strength H. The internal structure of a permeance block with hysteresis behavior is demonstrated in Fig. 3. The magnetomotive force F across the variable permeance component is measured and divided by the magnetic path length l, and yields the field strength H. The classical Preisach model is described in C-Script, which takes H as well as the flux rate $\dot{\Phi}$ as input variables. The C-Script outputs the instantaneous differential permeability $\mu(H) = dB/dH$, which is further on multiplied by the geometry factor A/l and provided to the variable permeance block. The calculation of $\mu(H)$ during simulation is introduced as follows.

1) *Virgin curve:* Assuming that the time-domain simulation initiates from the completely demagnetized state, the boundary between the positive (S_+) and negative area (S_-) of the Preisach plane lays on $U = -V$, such that the flux density B calculated using (1) is equal to 0, as depicted on the right-hand side of Fig. 4(a). Under positive excitation (e.g., with positive voltage applied on the winding of the magnetic component, so that $\dot{\Phi} > 0$), the operation point on the $B-H$ plane moves along the virgin curve, and the flux density B is calculated as the Everett integration following (1):

$$\begin{aligned} B(H) = &\iint_{S_+} p_s(U) \cdot p_s(-V) \cdot dU dV \\ &- \iint_{S_-} p_s(U) \cdot p_s(-V) \cdot dU dV. \end{aligned} \tag{4}$$

On the $B-H$ plane, the instantaneous differential permeability μ, or in other words, the slope of the $B-H$ curve, is graphically demonstrated on the left-hand side of Fig. 4(a) and given as

$$\mu_{\uparrow}(H) = 2 \cdot p_s(H) \cdot \int_{-H}^{+H} p_s(-V) \cdot dV. \tag{5}$$

In the above-mentioned equation, the integral term turns out to be of closed form if the PDF p_s can be analytically integrated, so as is the case of the Cauchy–Lorentz PDF, which has been adopted in the existing publications.

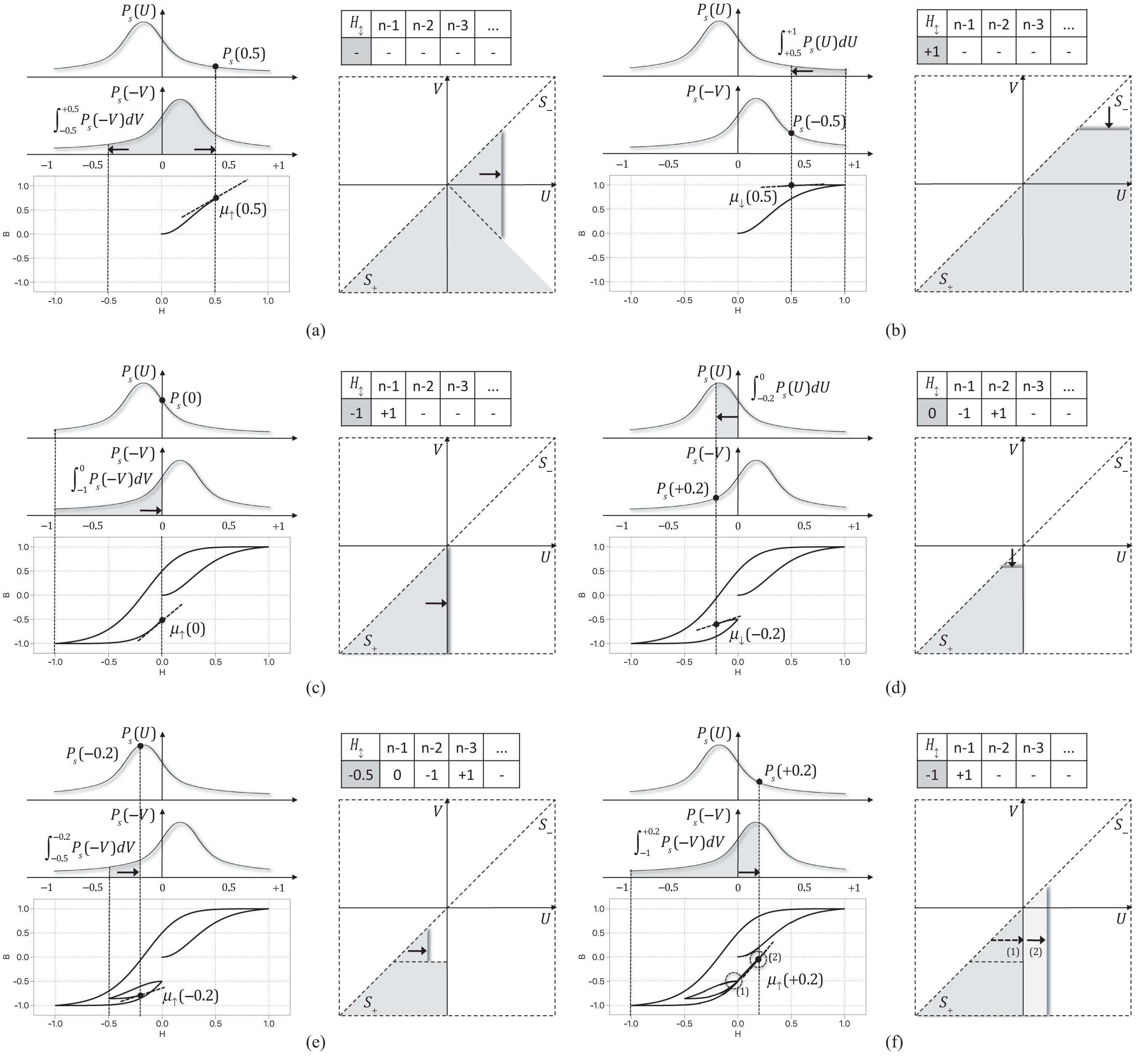

Fig. 4. Calculation of the permeability and the area separation of the Everett integral: (a) on the virgin curve; (b) on the descending curve after reaching the positive peak; (c) on the ascending curve after reaching the negative peak; (d) on the descending curve in an asymmetrical minor loop; (e) on the ascending curve in an asymmetrical minor loop; and (f) on the ascending curve after exiting the minor loop.

Thus μ with explicit expression can be directly substituted into (3) and assigned to the permeance core block of the magnetic circuit.

2) *Descending curve:* Assuming that when H reaches the positive peak (p.u. $+1$), the external excitation changes the polarity. Afterward, the boundary between the areas S_+ and S_- should move in the direction indicated on the right-hand side of Fig. 4(b). This polarity change is detected by the C-Script via examining the sign of the second input $\dot{\Phi}$ (time derivative of the flux Φ), and the first field strength extremity $+1$ is pushed into a stack structure, as shown on the top right of Fig. 4(b). From this time point on, μ is calculated using the following equation with extremity $H_\updownarrow = +1$:

$$\mu_\downarrow(H) = 2 \cdot p_s(-H) \cdot \int_{H}^{H_\updownarrow} p_s(U) \cdot dU. \tag{6}$$

3) *Ascending curve:* The external excitation becomes positive after H reaches the negative peak (p.u. -1), as shown in Fig. 4(c). The negative peak is pressed into the stack of extremities and the actual $H_\updownarrow$ becomes -1, meanwhile, the previous extremity $+1$ is shifted to a deeper level. The permeability on the ascending curve is given as follows:

$$\mu_\uparrow(H) = 2 \cdot p_s(H) \cdot \int_{H_\updownarrow}^{H} p_s(-V) \cdot dV. \tag{7}$$

4) *Minor loop:* The external excitation switches its polarity again to negative at $H = 0$ on the ascending curve, so that a minor hysteresis loop is initiated [see Fig. 4(d)]. At the very moment, $H_{\updownarrow}$ becomes 0, whereas the previous two extremities -1 and $+1$ are shifted one level deeper in the stack. The permeability on the descending curve of the minor loop has the same form as (6), except for the integral limit $H_{\updownarrow} = 0$. Afterward, let us assume that the ascending curve of the minor loop begins at $H = -0.5$ where $H_{\updownarrow}$ becomes -0.5 [see Fig. 4(e)]. Before H reaches the over last extremity ($H = 0$), there are four values in total $(-0.5, 0, -1, +1)$ stored in the stack, and μ is retained following (7) with $H_{\updownarrow} = -0.5$.
5) *Exit from minor loop:* At the moment when H just tends to exceed the over last extremity ($H = 0$), the operation point is exactly located on the position where the minor loop was initiated previously [point (1) in Fig. 4(f)]. At this time point, the latest two extremities -0.5 and 0 are erased from the stack. From then on, the operation point travels along the ascending curve with $H_{\updownarrow} = -1$, as if the minor loop has never happens [point (2) in Fig. 4(f)]. This deletion property of the Preisach model corresponds to the characteristic of ferrite material in reality, which will be verified by the experimental result in a later section of this paper.

III. Proposed Model

The main objective of the proposed modeling approach is to achieve good accuracy of simulating magnetic hysteresis in a wide range of amplitudes (both large major and small minor loops), which is evaluated by the two criteria mentioned below.

1) *Per-cycle energy loss:* The area enclosed by the hysteresis loops on the $B - H$ plane.
2) *Equivalent inductivity:* The slope of the virtual straight line connecting the positive and negative peaks.

For illustration purpose, the characteristic of ferrite material N87 experimentally measured at 200 Hz is taken as an example. In Fig. 5, the hysteresis loops of different amplitudes are displayed together. We define the one with the largest field strength amplitude $\hat{H}_{100\%}$ (e.g., 100 A/m), which makes the flux density approach saturation, as the "limiting loop." The "limiting loop" indicates the valid operation range of the model and it is assumed that the hysteresis effect is of concern only inside this range within the simulation. Inside the limiting loop, one can realize that peaks of the other loops with relatively large amplitudes $40\% \cdot \hat{H}_{100\%} \sim 80\% \cdot \hat{H}_{100\%}$ (40–80 A/m) almost attach on the lower boundary of the limiting loop. This phenomenon has also been observed from other ferrite materials, which indicates that if a simulation model is able to reproduce the lower boundary of the limiting loop, the smaller ones can be also well presented, at least in terms of the equivalent inductivity. However, this theory does not apply to the minor hysteresis loop with very low amplitude, say $20\% \cdot \hat{H}_{100\%}$ (20 A/m), whose peaks obviously deviate from the lower boundary of the limiting loop.

In the approach proposed in this paper, only one limiting hysteresis loop [see Fig. 6(a)] and one symmetrical minor hysteresis loop [see Fig. 6(c)] are required to be experimentally measured as input, and the model is parameterized to approximate these two loops. We suppose the hysteresis loops with amplitudes between the measured limiting and minor loops can be automatically fitted, thanks to the physical-based intrinsic property of the Preisach model, which will be verified in a later section via experimental tests.

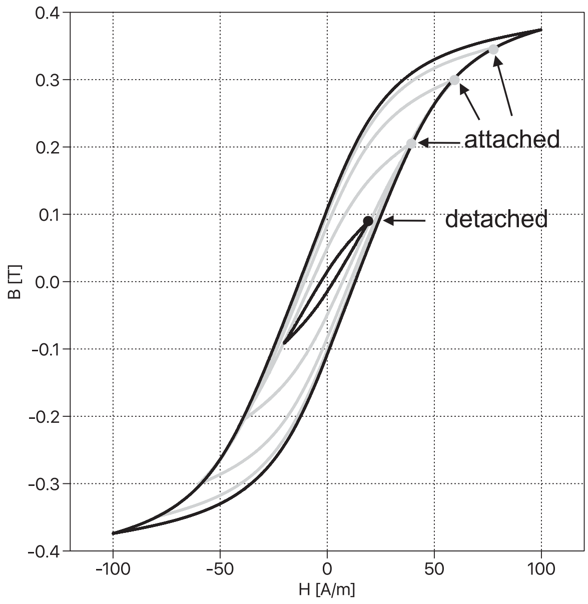

Fig. 5. Measured hysteresis loops of ferrite material N87 from $H = 100$ to $H = 20$ A/m at 200 Hz.

Following the method proposed by Torre *et al.* [23], in this paper, we also construct the hysteresis model as the summation of an irreversible and a reversible component, which is graphically demonstrated in Fig. 6(b) and (d) for the limiting loop and the minor loop, respectively. Please note that the same classical Preisach model is applied for the irreversible component, and the reversible component in Fig. 6(d) is just one part of the same curve in Fig. 6(b), within the field strength range $[-H_{20\%}, +H_{20\%}]$. The formulation and parameter identification of the two components are introduced in the following sections.

A. Determination of the Irreversible Component

Contrary to the existing publications, the "logistic" PDF is adopted for the irreversible component, which is represented by the classical Preisach model. The generalized form of the logistic PDF can be expressed as follows:

$$p_s(H) = K \cdot \frac{e^{-(H-H_0)\cdot\sigma}}{(1 + e^{-(H-H_0)\cdot\sigma})^2} \tag{8}$$

where K, H_0, and σ are parameters to be determined. Similar to the Cauchy–Lorentz PDF, which has been chosen by the existing publications, the logistic PDF can be integrated analytically, thus the cumulative distribution function of the logistic PDF is given as follows:

$$C_s(H) = \frac{K \cdot \sigma}{1 + e^{-(H-H_0)\cdot\sigma}}. \tag{9}$$

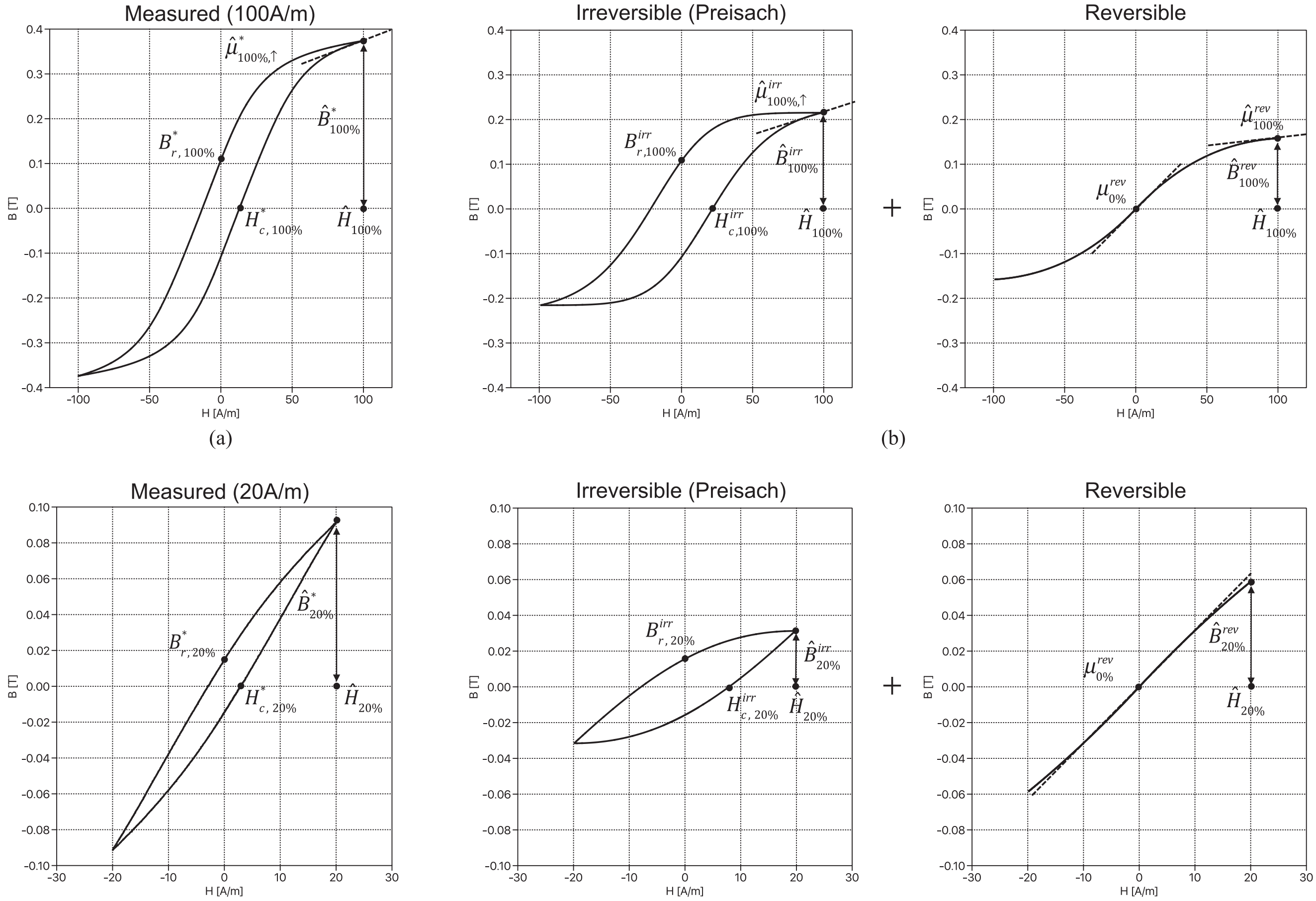

(a)

(b)

(c)

(d)

Fig. 6. (a) Measured limiting hysteresis loop with amplitude $H_{100\%} = 100$ A/m. (b) Hysteresis model composed of irreversible and reversible components with amplitude $H_{100\%} = 100$ A/m. (c) Measured limiting hysteresis loop with amplitude $H_{20\%} = 20\% \cdot H_{100\%} = 20$ A/m. (d) Hysteresis model composed of irreversible and reversible components with amplitude $H_{20\%} = 20\% \cdot H_{100\%} = 20$ A/m.

In this way, the permeability μ can be calculated in a closed form (5)–(7). Due to the fact that the reversible component has zero remanence, the remanent flux density of the simulated irreversible component [$B^{\text{irr}}_{r,100\%}$ in Fig. 6(b) and $B^{\text{irr}}_{r,20\%}$ in Fig. 6(d)] must be equal to that of the measurement

$$\text{Conditions} \begin{cases} B^{\text{irr}}_{r,100\%} \triangleq B^*_{r,100\%} \\ B^{\text{irr}}_{r,20\%} \triangleq B^*_{r,20\%} \end{cases} \tag{10}$$

where $B^*_{r,100\%}$ and $B^*_{r,20\%}$ are the remanent flux density of the measured limiting and minor loops, as has been highlighted in Fig. 6(a) and (c), and any values from experimental measurement in this paper are denoted with superscript "*". As has been explored by Cardelli *et al.* [27], the remanence flux density of the Preisach model using an independent PDF can be explicitly expressed by

$$\begin{aligned} B^{\text{irr}}_{r,100\%} &= \int_0^{\hat{H}_{100\%}} p_s(U)dU \int_{-\hat{H}_{100\%}}^0 p_s(-V)dV \\ &= (C_s(\hat{H}_{100\%}) - C_s(0))^2 \triangleq B^*_{r,100\%}. \end{aligned} \tag{11}$$

The above-mentioned is also valid for the symmetrical minor loop

$$\begin{aligned} B^{\text{irr}}_{r,20\%} &= \int_0^{\hat{H}_{20\%}} p_s(U)dU \int_{-\hat{H}_{20\%}}^0 p_s(-V)dV \\ &= (C_s(\hat{H}_{20\%}) - C_s(0))^2 \triangleq B^*_{r,20\%}. \end{aligned} \tag{12}$$

Apart from the metal-based materials, since ferrite materials do not undertake field-annealing treatment during the manufacture process, it is reasonable to assume symmetrical nature for the PDF of the classical Preisach model. Therefore, the bias parameter H_0 of the irreversible part (8) and (9) is chosen to be 0 in this paper, which makes the PDF be symmetrical about the vertical axis. In this way, the remaining two parameters K and σ can be fully determined via solving (11) and (25). Due to nonlinearity, commonly used iteration method such as Newton-Raphson can be adopted. Please note that the per-cycle energy loss is controlled by the irreversible component.

B. Determination of the Reversible Component

After the Preisach model parameters of the irreversible component (the classical Preisach model) are identified, the reversible component is parameterized to make the summation of the two components with the same peak point as the measured limiting and minor loops, or in other words, to control the equivalent permeability of them. Instead of $\arctan$ and $\coth$ proposed by the existing publications, a new form of "Sigmoid" function is proposed in this paper, in order to shape the reversible component with more degrees of freedom. The reversible $B^{\text{rev}}(H)$ is constructed as the integration of a shifted $\arctan$ function, and the flux density when $H \geq 0$ is governed by the following equation:

$$\begin{aligned} B^{\text{rev}}(H) &= \int_0^H \Big(F \cdot \arctan\left((H_1 - x) \cdot \alpha\right) + D\Big) dx \\ &= -F/\alpha \cdot \big((H_1 - H) \cdot \alpha \cdot \text{atan}\left((H_1 - H) \cdot \alpha\right) - 0.5\text{ln} \\ &\quad (1 + (H_1 - H)^2 \cdot \alpha^2)\big) + F\alpha \cdot \big(H_1 \cdot \alpha \cdot \text{atan}\left(H_1 \cdot \alpha\right) \\ &\quad + 0.5\text{ln}(1 + H_1^2 \cdot \alpha^2)\big) + D \cdot H. \end{aligned} \tag{13}$$

The permeability $\mu^{\text{rev}}(H)$ to be provided to the permeance block in the magnetic circuit is the derivative of (13) about field strength H, or in other words, the shifted $\arctan$ function itself

$$\mu^{\text{rev}}(H) = F \cdot \arctan((H_1 - H) \cdot \alpha) + D. \tag{14}$$

In the operation range with field strength $H < 0$, the mirror of (13) and (14) about the origin of the $B - H$ plane are applied. The parameter α is preliminary configured to be 0.01 and can be adjusted to improve the permeability accuracy, which will be described later in Section III-C. The identification of the other three parameters H_1, F, and D is described in the following.

In the Preisach model, the symmetry of the irreversible component's PDF (due to the parameter configuration $H_0 = 0$) leads to the fact that the peak flux density $\hat{B}^{\text{irr}}_{100\%}$ of the simulated limiting loop is two times the remanent flux density $B^{\text{irr}}_{r,100\%}$ (equal to $B^*_{r,100\%}$) after the parameter identification described in Section III-A

$$\hat{B}^{\text{irr}}_{100\%} = 2 \cdot B_{r,100\%} \overset{\Delta}{=} 2 \cdot B^*_{r,100\%}. \tag{15}$$

Therefore, the peak flux density of the reversible component at $\hat{H}_{100\%}$ can be extracted from the measured peak flux density of the limiting loop, given by

$$\hat{B}^{\text{rev}}_{100\%} = B^*_{100\%} - \hat{B}^{\text{irr}}_{100\%} = B^*_{100\%} - 2 \cdot B^*_{r,100\%}. \tag{16}$$

As has been observed at the beginning of Section III, the peak of the relatively large minor loops attaches the lower boundary of the limiting loop. In order to make the simulated lower boundary of the limiting loop close to that from the measurement, the permeability of the reversible component at $\hat{H}_{100\%}$ [$\hat{\mu}^{\text{rev}}_{100\%}$ in Fig. 6(b)] should be controlled as well, which is given by subtracting the permeability of the irreversible component model from the measured one

$$\begin{aligned} \hat{\mu}^{\text{rev}}_{100\%} &= \hat{\mu}^*_{100\%} - \hat{\mu}^{\text{irr}}_{100\%} \\ &= \hat{\mu}^*_{100\%} - p_s(\hat{H}_{100\%})(C_s(\hat{H}_{100\%}) - C_s(-\hat{H}_{100\%})). \end{aligned} \tag{17}$$

In the case of the minor symmetrical loop with field strength amplitude $\hat{H}_{20\%} = 20\% \cdot \hat{H}_{100\%}$, the irreversible component described by the Preisach model is calculated using solely the part of the PDF inside the range $[-\hat{H}_{20\%}, +\hat{H}_{20\%}]$. With the previous assumption $H_0 = 0$, this part of the PDF is also symmetrical about origin, so that the relation described in (15) is valid here as well

$$\hat{B}^{\text{irr}}_{20\%} = 2 \cdot B_{r,20\%} \overset{\Delta}{=} 2 \cdot B^*_{r,20\%}. \tag{18}$$

If the reversible component can be considered as a linear function close to origin, as depicted in Fig. 6(d), the initial permeability of the reversible component can be obtained via subtracting $\hat{B}^{\text{irr}}_{20\%}$ from the peak flux density of the measured minor loop and dividing by $\hat{H}_{20\%}$

$$\mu^{\text{rev}}_{0\%} = (\hat{B}_{20\%} - \hat{B}^{\text{irr}}_{20\%})/\hat{H}_{20\%} = (\hat{B}^*_{20\%} - 2 \cdot B^*_{r,20\%})/\hat{H}_{20\%}. \tag{19}$$

Up to this stage, with the parameter α given, the other three parameters H_1, F, and D of the reversible component can be determined via solving (16), (17), and (19), and substituting $\hat{B}^{\text{rev}}_{100\%}$, $\hat{\mu}^{\text{rev}}_{100\%}$, and $\mu^{\text{rev}}_{0\%}$ by the expressions from (13) and (14). The Newton–Raphson iteration is adopted for the parameter identification and initial values should be configured to guarantee the convergency

$$\begin{cases} H_1^{(0)} = \dfrac{\hat{B}^{\text{rev}}_{100\%} - \hat{H}_{100\%} \cdot \hat{\mu}^{\text{rev}}_{100\%}}{\mu^{\text{rev}}_{0\%} - \hat{\mu}^{\text{rev}}_{100\%}} \\ K^{(0)} = \dfrac{\mu^{\text{rev}}_{0\%} - \hat{\mu}^{\text{rev}}_{100\%}}{v_1 - v_2} \\ D^{(0)} = \dfrac{\mu^{\text{rev}}_{0\%} \cdot v_2 - \hat{\mu}^{\text{rev}}_{100\%} \cdot v_1}{v_2 - v_1} \end{cases} \tag{20}$$

where $\hat{B}^{\text{rev}}_{100\%}$, $\hat{\mu}^{\text{rev}}_{100\%}$, and $\mu^{\text{rev}}_{0\%}$ are given by the right-hand side of (16), (17), and (19), respectively, whereas v_1 and v_2 are provided as follows:

$$v_1 = \arctan\left(H_1^{(0)} \cdot \alpha\right) \tag{21}$$

$$v_2 = \arctan\left((H_1^{(0)} - \hat{H}_{100\%}) \cdot \alpha\right). \tag{22}$$

C. Final Adjustment

For the sake of further controlling the simulated lower boundary of the limiting loop to approach that from the measurement, which intrinsically determines the peak point of the other minor loops with amplitude close to the limiting loop (as has been discussed in Fig. 5), the parameter α can be adjusted.

The goal is to make the simulated flux density $B_{50\%}$ at $H_{50\%} = 0.5 \cdot \hat{H}_{100\%}$ be equal to that on the limiting loop's ascending curve. The parameter α determines the curvature of the reversible component such that the flux density $B^{\text{rev}}_{50\%}$ at $H_{50\%}$ on the reversible component can be adjusted via changing α, as demonstrated in Fig. 7(a). In Fig. 7(a), the Newton–Raphson iteration described in Section III-B should be carried out for any adopted α value, so that the point $\hat{B}^{\text{rev}}_{100\%}$ as well as the slopes $\hat{\mu}^{\text{rev}}_{100\%}$ and $\mu^{\text{rev}}_{0\%}$ remains the same. Please note that at this stage, the irreversible component has been completely determined and its parameter remains unchanged, which leads to the fact that the change of $B^{\text{rev}}_{50\%}$ due to adjustment of α is directly reflected on $B_{50\%}$, which locates on the lower boundary of the simulated limiting loop, as shown in Fig. 7(b).

For parameterization of the parameter α, the direct objective is to have the reversible flux density $B^{\text{rev}}_{50\%}$ at $H_{50\%}$ [obtained

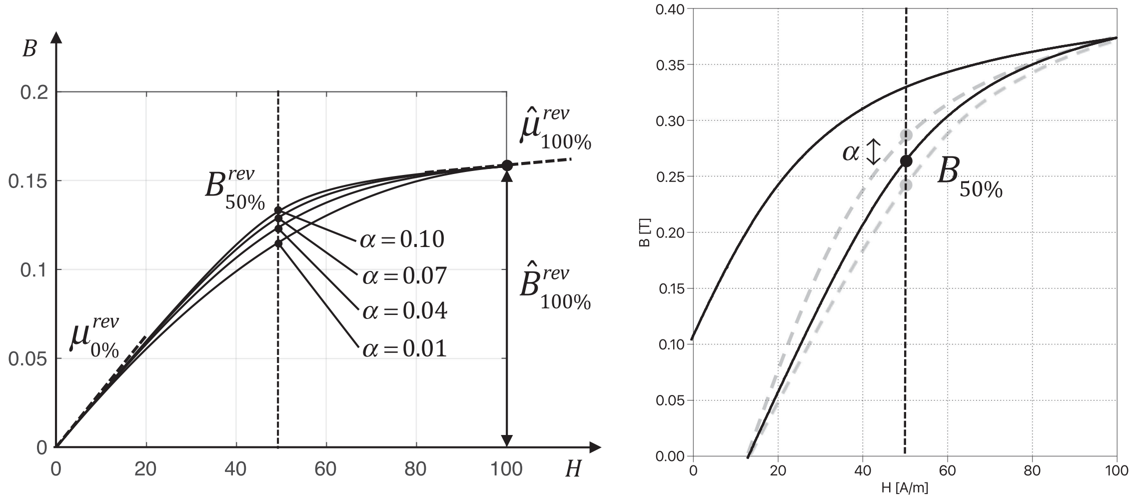

(a) (b)

Fig. 7. (a) Influence of the model parameter α on the curvature of the irreversible component. (b) Influence of the model parameter α on the lower boundary of the limiting hysteresis loop after summing up the reversible and irreversible component together.

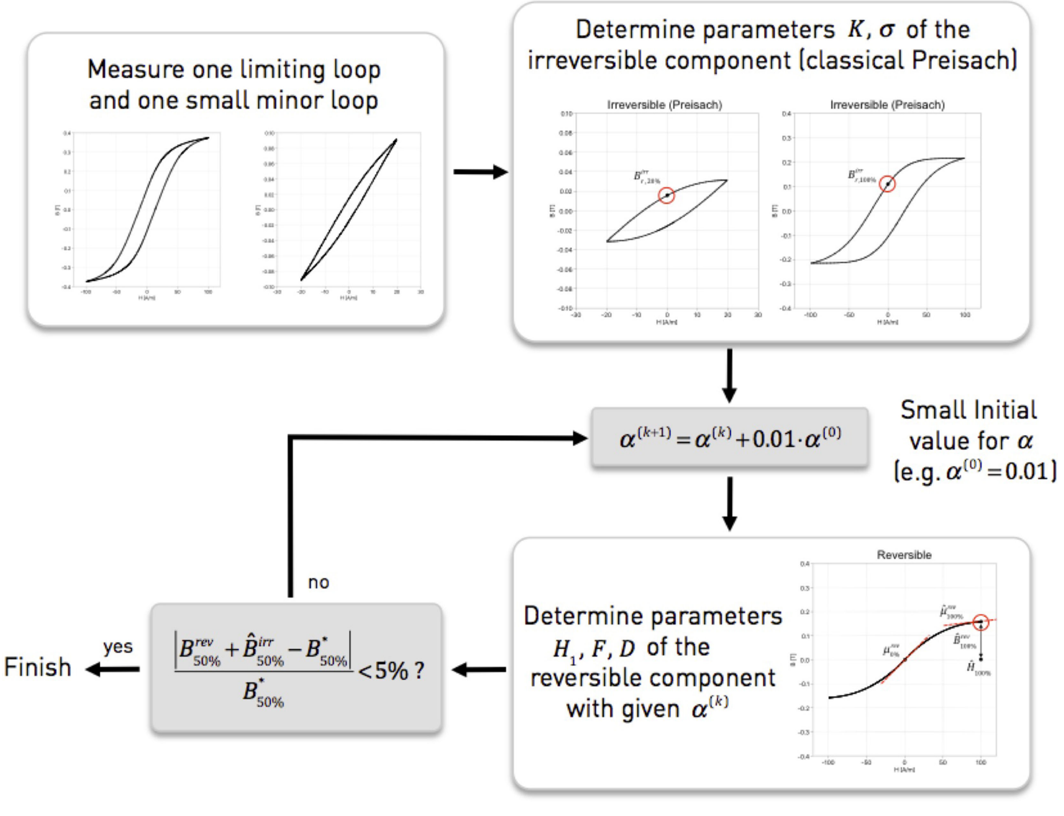

Fig. 8. Parameterization of the proposed model including the iteration to determine the parameter α.

from (13)] plus the peak flux density $\hat{B}^{\text{irr}}_{50\%}$ of the simulated irreversible hysteresis loop with field strength amplitude $H_{50\%}$ be equal to the flux density $B^*_{50\%}$ at $H_{50\%}$ on the ascending branch of the measured limiting loop

$$B^{\text{rev}}_{50\%} + \hat{B}^{\text{irr}}_{50\%} \overset{\Delta}{=} B^*_{50\%}. \tag{23}$$

Since the relationship between the remanence and peak flux density presented in (15) and (18) is also valid for the irreversible hysteresis loop with field strength amplitude $H_{50\%}$, the peak flux density $\hat{B}^{\text{irr}}_{50\%}$ from (23) is given by

$$\hat{B}^{\text{irr}}_{50\%} = 2 \cdot B_{r,50\%}. \tag{24}$$

Following the same formulation from (11) and (25), $B_{r,50\%}$ can be explicitly expressed as

$$B_{r,50\%} = (C_s(\hat{H}_{50\%}) - C_s(0))^2. \tag{25}$$

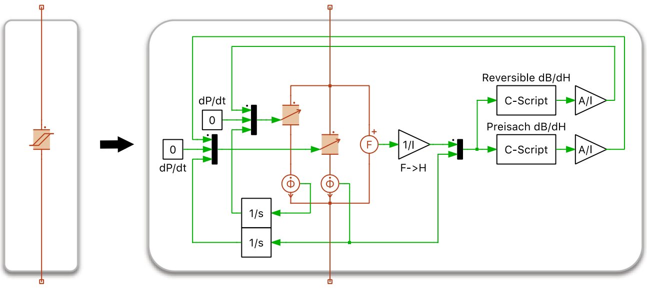

Fig. 9. Model structure of the permeance block using the proposed model.

Thanks to the fact that α is monotonously related to $B^{\mathrm{rev}}_{50\%}$ ($B^{\mathrm{rev}}_{50\%}$ increases with higher α), the adjustment of α can be easily conducted either manually or automatically via adding another fitting loop on the top of the Newton–Raphson iteration introduced in Section III-B, as illustrated in Fig. 8. After the parameters of the irreversible component are determined (see Section III-A), a small initial value is configured to the parameter α (e.g., $\alpha^{(0)}$=0.01), so that the left-hand side of (23) is lower than the measured $B^{*}_{50\%}$. Then, a simple iterative process is started, in each cycle α is added up with a small increment of $0.01 \cdot \alpha^{(0)}$, and the parameters H_1, F, and D are obtained with the new α using Newton–Raphson iteration (see Section III-B). At the end of each cycle, the left-hand side of (24) is evaluated and compared to the measured $B^{*}_{50\%}$. The iteration is terminated as soon as the error becomes lower than 5%.

D. Model Structure

The structure of the proposed combined hysteresis model in a permeance–capacitance based magnetic circuit is shown in Fig. 9. Two variable core blocks are connected in parallel, to account for the irreversible and reversible components, respectively. The permeance value of the two core blocks is calculated in two separate C-Scripts and scaled with the geometric coefficient A/l. The equivalent permeance of the whole hysteresis core block isessentially the sum of the individual permeances, which are provided to the first input of the variable core blocks

$$\mathscr{P}(H) = \mu^{\mathrm{irr}}(H) \cdot \frac{A}{l} + \mu^{\mathrm{rev}}(H) \cdot \frac{A}{l}. \tag{26}$$

Since differential permeability has been used throughout this paper, the second input of the variable core blocks $d\mathscr{P}/dt$ can be provided by a constant zero, as has been discussed in [3]. The third input of the variable core blocks accepts the flux density of the irreversible and reversible components, which are obtained from integral of the flux rate $\dot{\Phi}$, in order to make the simulation solver hold Kirchhoff's junction law for the magnetic circuit.

IV. VERIFICATION IN CONTINUOUS CIRCUIT

For validation of the proposed modeling approach, a test bench based on the two-winding approach described in [28] has been established to measure the hysteresis loop of the core materials, as shown in Fig. 10(a) and (b). Since geometry impact is not in scope of this paper, only toroidal core is considered, which is sufficiently representative for the material's characteristic. The toroidal core sample is equipped with two windings, the primary winding is supplied by an RF power amplifier (type LM3886, gain bandwidth product 2 MHz), which generates sinusoidal voltage excitation. A shunt resistor together with its instrumentation amplifier circuitry is installed on the primary side to measure the current I, which is converted into field strength using the following equation:

$$H = \frac{I \cdot N_1}{l} \tag{27}$$

where l is the equivalent magnetic path length of the core sample and N_1 the turns number of the primary winding. The secondary winding is left open and the voltage is measured using a resistor divider. The measured voltage is integrated to obtain the flux density given by

$$B = \frac{1}{A \cdot N_2} \int U dt \tag{28}$$

where A is the equivalent cross-sectional area of the core sample, and N_2 the turns number of the secondary winding. A control unit (PLECS RT-Box 1) is connected to the test bench to generate reference signal for power amplifier and process the measurements. As this paper focuses on the frequency independent hysteresis effect without eddy current and residual effects, the power amplifier's output voltage has been configured as low-frequency 200 Hz sinusoidal wave. As the temperature dependence is also not in the scope of this paper, all tests have been conducted under room temperature of 25 °C.

The simulation model [top of Fig. 10(b)] is established in the system-level simulation software PLECS for power electronics. The hysteresis core block represents the core sample, whose geometric parameters A and l are configured using the values from the datasheet, whereas the material characteristic is modeled and parameterized using the approach introduced in Section III. The power amplifier is modeled as an ideal sinusoidal ac voltage source, in series to which the equivalent resistance (including the shunt resistor for current measurement and parasitics, measured in dc condition) is connected. All components are configured to match the test bench hardware.

The ferrite material N87 from TDK is taken as the first verification case, where the toroidal core of size code "R 41.8 × 26.2 × 12.5" is taken as a sample, and the turns number of primary and secondary windings are both eight. As the input of the parameter identification process, which is introduced in Section III, the limiting hysteresis loop with amplitude $\hat{H}_{100\%} =$ 100 A/m and a symmetrical minor loopwith amplitude $\hat{H}_{20\%}$ are measured. Please note that the parameters of the model will remain the same in the other verification cases. In Fig. 11(a) and (b), the simulated hysteresis loop as well as the time-domain waveform of the primary winding current and secondary winding voltage at different field strength amplitudes (20–100 A/m) are compared to the experimental measurement. Although an ideal sinusoidal voltage is generated on the power amplifier output, the measured primary winding current is heavily distorted, due to the presence of nonlinear hysteresis effect. The proposed simulation model is able to approximate the hysteresis loop on the *B*–*H* plane as well as the time-domain waveform well. Especially on the secondary voltage waveform

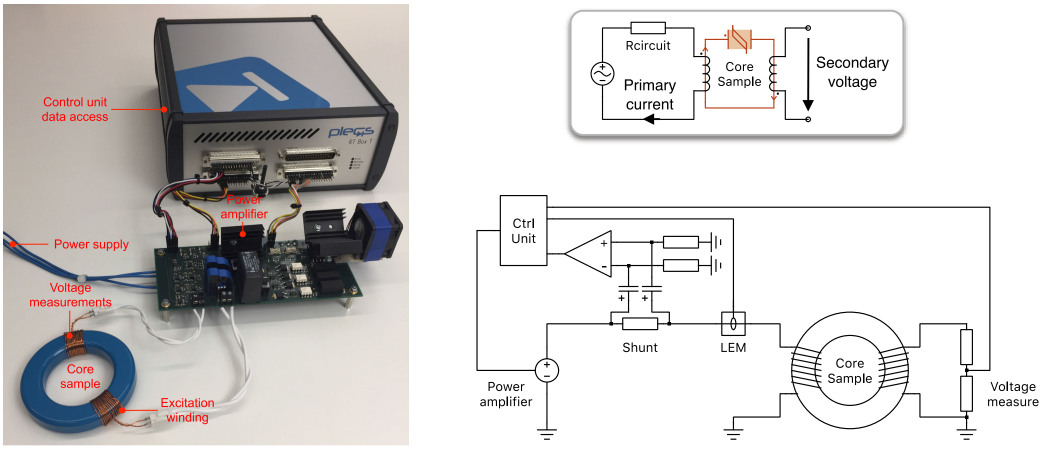

(a) (b)

Fig. 10. (a) Hardware configuration of the test setup. (b) Schematic and simulation model of the test setup.

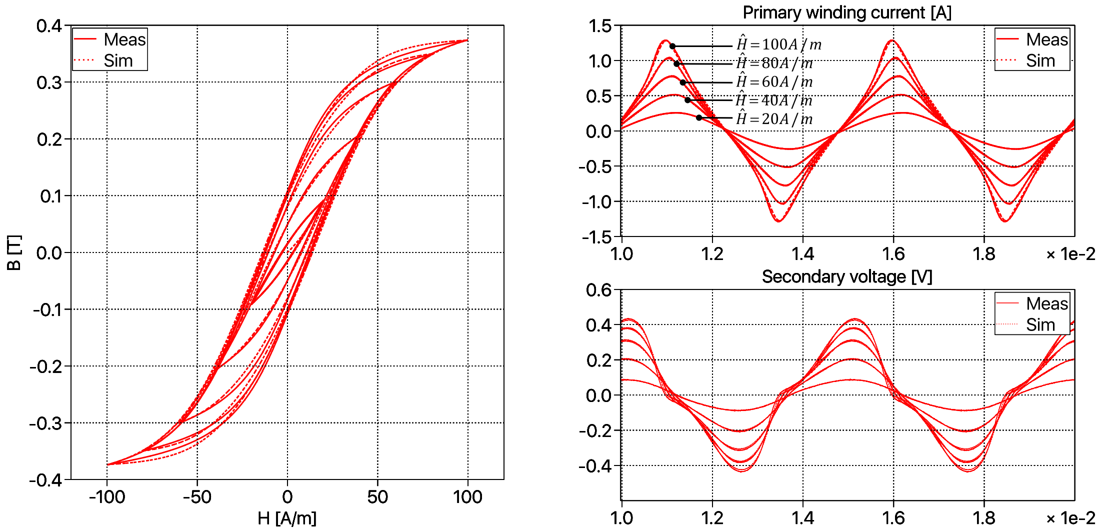

(a) (b)

Fig. 11. Comparison between measurement and simulation of Ferrite N87 at different field strength amplitudes. (a) Hysteresis loop. (b) Time-domain primary winding current and secondary voltage.

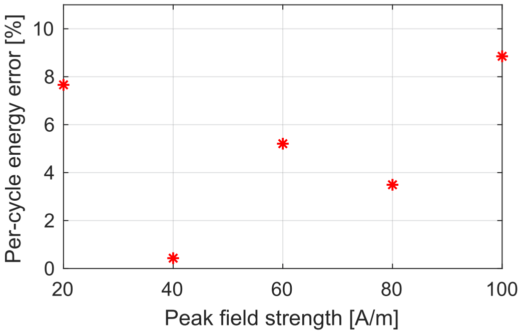

Fig. 12. Percentage error of the simulated per-cycle energy loss from simulation of ferrite N87.

in Fig. 11(b), due to voltage drop on the circuit resistance as a coupled effect from the distorted circuit current, the secondary open-circuit voltage also includes harmonic component, which is captured by the model as well. In Fig. 11(a), the peak point of the hysteresis loops nearly overlaps with the measurement,

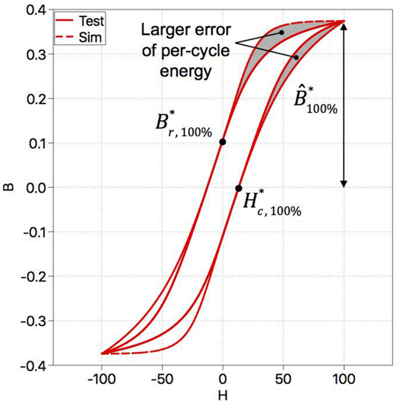

Fig. 13. Comparison of the limiting hysteresis loop between measurement and simulation using only the classical Preisach model without the reversible component.

so that the error of the equivalent permeability is maintained under 1%. The per-cycle energy loss has been measured and simulated via integrating the product of time-domain

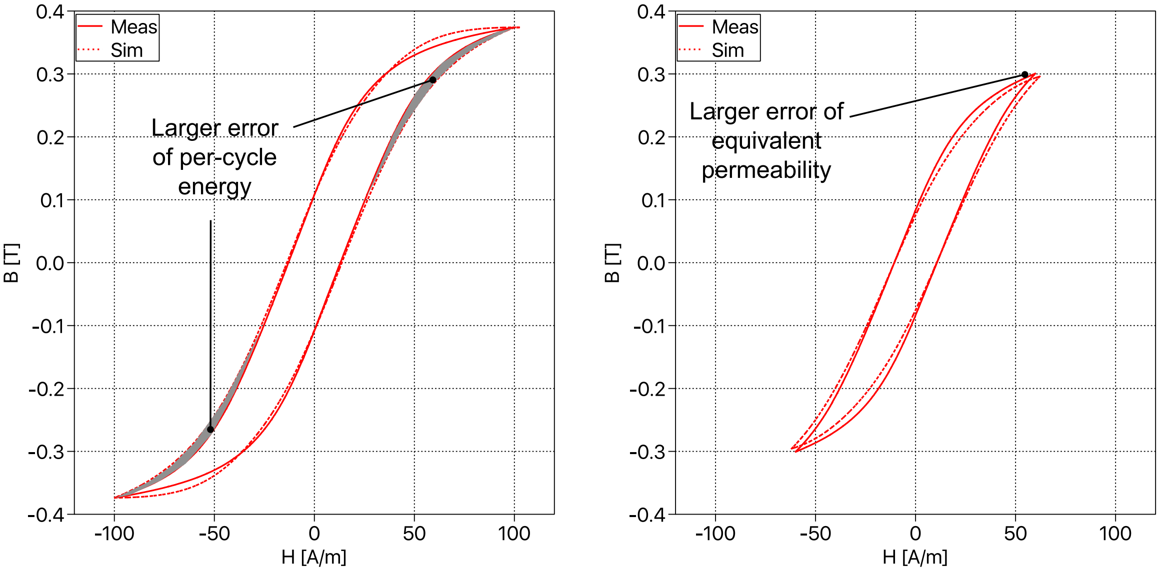

(a) (b)

Fig. 14. Comparison between measurement and simulation of Ferrite N87 using the Cauchy–Lorentz PDF. (a) Hysteresis loop at $\hat{H}_{100\%} = 100$ A/m. (b) Hysteresis loop at $\hat{H}_{60\%} = 60$ A/m.

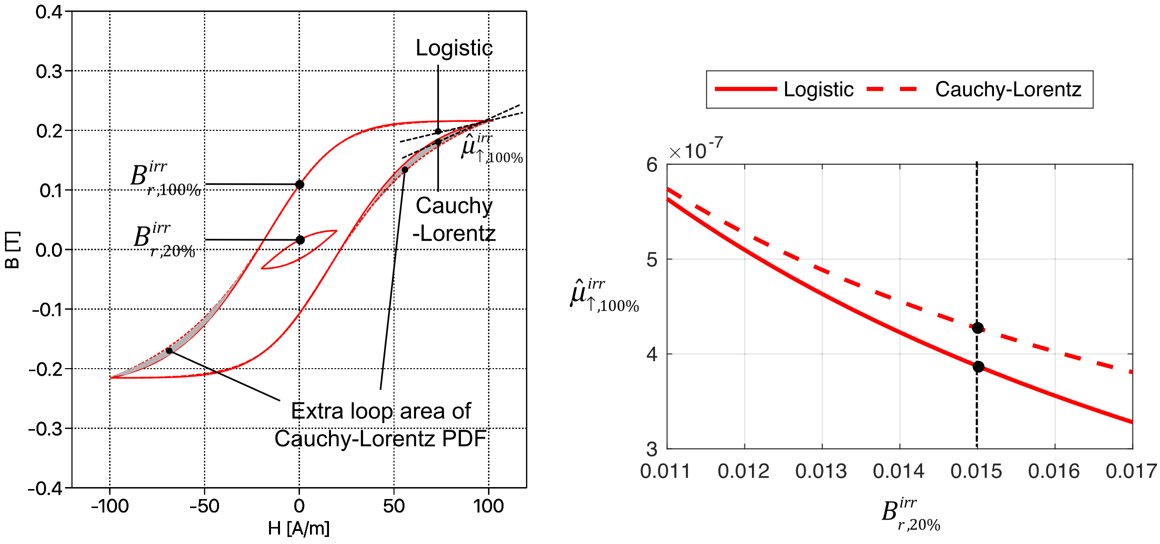

(a) (b)

Fig. 15. Comparison of irreversible component between the Preisach model using two different PDFs. (a) Irreversible component with field strength amplitude $\hat{H}_{100\%} = 100$ A/m. (b) Permeability on the top of the ascending branch of a limiting loop with model parameters fitted to fixed $B^{\mathrm{irr}}_{r,100\%}$ and varying $B^{\mathrm{irr}}_{r,20\%}$.

voltage and current waveform for one ac period (equivalent to the enclosed area of the B–H loop), whose error between simulation and measurement is listed in Fig. 12. The maximum error 8.9% is present at the limiting hysteresis loop of high amplitude $\hat{H}_{100\%} = 100$ A/m, whereas the error at the other operation points are all controlled below 10%.

For comparison purpose, only the irreversible classical Preisach model using the Cauchy–Lorentz PDF (shown in Fig. 3) is parameterized to approximate the peak flux density $\hat{B}^{*}_{100\%}$, remanence flux density $B^{*}_{r,100\%}$, and the coercitive field strength $H^{*}_{c,100\%}$ of the measured limiting loop, following the method introduced in [3]. The simulated B–H characteristic exhibits significant larger loop area compared to the measurement, which results in much higher per-cycle energy loss (error over 30%), as demonstrated in Fig. 13.

With the proposed reversible component included, if the irreversible component is calculated using the Cauchy–Lorentz PDF (adopted by [12]) whose parameters are identified following the same procedure described in Section III-A, the hysteresis loops with field strength amplitude of 100 A/m (limiting loop) and 60 A/m are compared to the measurement in Fig. 14(a) and (b), respectively.

In Fig. 14(a), the simulated limiting loop (at $\hat{H}_{100\%} =$ 100 A/m) using the Cauchy–Lorentz PDF exhibits significantly higher per-cycle energy loss, in comparison to the one using the logistic PDF [see Fig. 11(a)]. The excessive energy loss is

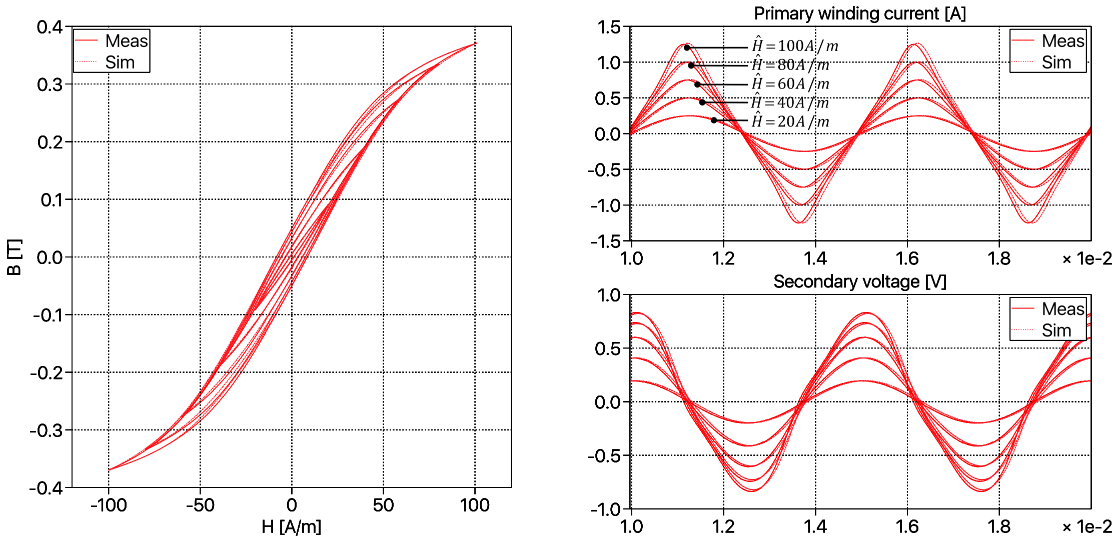

(a) (b)

Fig. 16. Comparison between measurement and simulation of Ferrite 3C81 at different field strength amplitudes. (a) Hysteresis loop. (b) Time-domain primary winding current and secondary voltage.

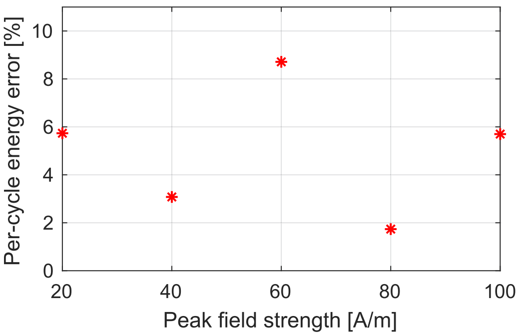

Fig. 17. Percentage error of the simulated per-cycle energy loss from simulation of ferrite 3C81.

indicated by the highlighted loop area difference (gray color). The error compared to the measurement is 11.5%, which is higher than that obtained using the logistic PDF (8.9%). The reason can be ascribed to the simulated differential permeability on the top of an ascending branch. The simulated irreversible component of the limiting loop (that of the right-hand-side variable permeance block in Fig. 9) is compared between the models using the logistic PDF and the Cauchy–Lorentz PDF in Fig. 15(a); higher permeability $\hat{\mu}^{\mathrm{irr}}_{\uparrow,100\%}$ is present on the model using the Cauchy–Lorentz PDF, which leads to a large enclosed area on the *B*–*H* plane, and thus higher per-cycle energy loss.

One should recall that in the parameter identification procedure from Section III-A, the irreversible component is configured to approximate the remanent flux density of the limiting loop and that of a low-amplitude minor loop, so that $B^{\mathrm{irr}}_{r,100\%} = B^{*}_{r,100\%}$ and $B^{\mathrm{irr}}_{r,20\%} = B^{*}_{r,20\%}$. To generalize the statement that $\hat{\mu}^{\mathrm{irr}}_{\uparrow,100\%}$ using the Cauchy–Lorentz PDF is higher than that using the logistic PDF; we fit the parameters of the irreversible component such that the remanent flux density of the limiting loop $B^{\mathrm{irr}}_{r,100\%}$ is still equal to the measurement, whereas that of the low-amplitude minor loop $B^{\mathrm{irr}}_{r,20\%}$ is fitted targeting different values. The resulted permeability $\hat{\mu}^{\mathrm{irr}}_{\uparrow,100\%}$ from the model using two PDFs are compared in Fig. 15(b), independent of $B^{\mathrm{irr}}_{r,20\%}$; the permeability $\hat{\mu}^{\mathrm{irr}}_{\uparrow,100\%}$ from the model using the Cauchy–Lorentz PDF is always higher than that using the logistic PDF, which leads to a higher per-cycle energy loss in simulation.

Moreover, in the case of N87 material, since the irreversible permeability $\hat{\mu}^{\mathrm{irr}}_{\uparrow,100\%}$ calculated using the Cauchy–Lorentz PDF is already higher than the permeability $\hat{\mu}^{*}_{\uparrow,100\%}$ from the measurement [in Fig. 6(a)], no positive permeability of the reversible component can be found to fulfill the criteria defined in (17). In this way, the lower boundary of the ascending curve of the model deviates from the measurement, which make the equivalent permeability of the minor loops (with amplitudes slightly lower than the limiting loop) to be less accurate, as has been highlighted in Fig. 14(b) on the hysteresis loop with field strength amplitude $\hat{H}_{60\%} = 60$ A/m. This permeability discrepancy together with the coupling from the circuit (e.g., voltage drop on the circuit resistance) adds up to the error of per-cycle energy loss.

Further on, the proposed model is verified on the 3C81 material from Ferroxcube, the core sample of shape code “TX51/32/19” is taken, whereas the turns number of both primary and secondary windings are 10. The parameters are identified based on the limiting hysteresis loop with amplitude $\hat{H}_{100\%} = 100$ A/m and a symmetrical minor loop with amplitude $\hat{H}_{20\%} = 20$ A/m. The comparison between simulation and measurement is presented in Fig. 16(a) and (b). Significantly, different shapes of hysteresis loop than N87 is present here and the proposed model is still able to approximate the measurement well. Again, the error of equivalent permeability is negligible, as in the case of N87, thanks to the proposed formulation of the

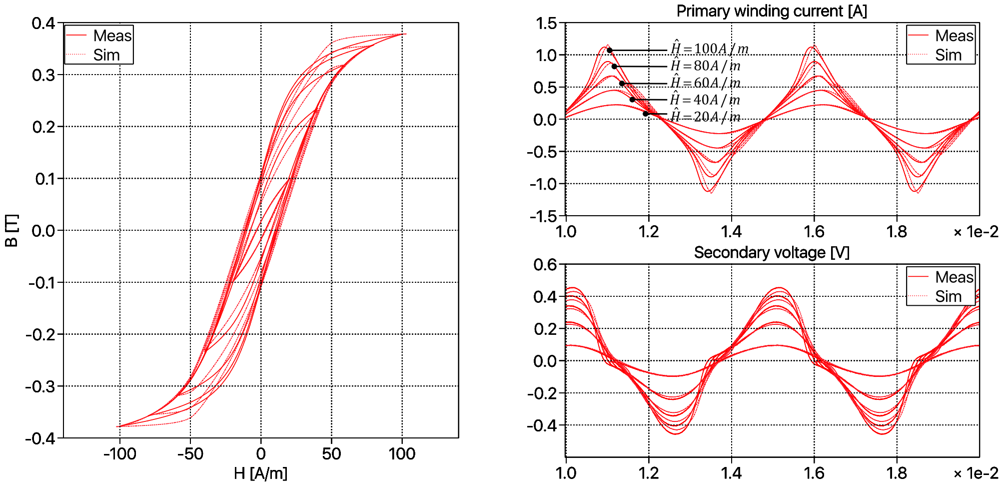

(a) (b)

Fig. 18. Comparison between measurement and simulation of Ferrite 3F3 at different field strength amplitudes. (a) Hysteresis loop. (b) Time-domain primary winding current and secondary voltage.

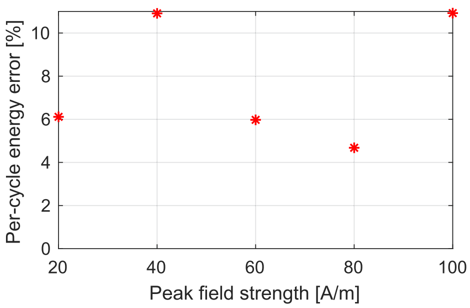

Fig. 19. Percentage error of the simulated per-cycle energy loss from simulation of ferrite 3F3.

reversible component. The maximum error of per-cycle energy loss is 8.7% at $\hat{H}_{60\%} = 60$ A/m, whereas the error of all the other loops are under 8%, as shown in Fig. 17.

The third material chosen for verification is 3F3 from Ferroxcube and the core sample is “TX36/23/15,” the turns number of both primary and secondary windings are 8. The parameters are also identified based on the limiting hysteresis loop with amplitude $\hat{H}_{100\%} = 100$ A/m and a symmetrical minor loop with amplitude $\hat{H}_{20\%} = 20$ A/m. Again, in Fig. 18(a) and (b), the comparison between simulation and measurement is presented. Larger shape discrepancy than the previous two materials can be observed in Fig. 18(a) at high field strength amplitudes (e.g., 100 A/m), due to the larger curvature of the 3F3 material’s hysteresis loop, whereas the accuracy of the equivalent permeability is still well controlled, thanks to the good approximation of the limiting loops’s lower boundary. The error of per-cycle energy loss is illustrated in Fig. 19, and the maximum value 10.9% of it occurs on the limiting loop with field amplitude $\hat{H}_{100\%} = 100$ A/m.

V. APPLICATION IN POWER ELECTRONIC CIRCUIT

In this section, the application of the proposed model in power electronic circuit is demonstrated. Another test setup has been constructed, as shown in Fig. 20(a) and (b). The same core sample of N87 ferrite from Section IV is adopted, which is equipped with two windings of eight turns each. On the left-hand side of the primary winding, the structure remains the same as the setup introduced in Section IV, which consisted of a power amplifier and shunt resistor for current measurement. On the right-hand side, a MOSFET half-bridge is additionally connected, whose dc side is supplied by other two power amplifiers. The circuit simulation model is established according to the test setup, as demonstrated on the top of Fig. 20(b), including the ac voltage source representing the output of the left-hand-side power amplifier, the circuit resistance of 0.4 Ω (measured under dc condition) as well as the MOSFET bridge supplied by two dc sources.

The first scheme tends to imitate the ferrite material’s operation in an isolation transformer of a dc–dc converter. The left-hand-side power amplifier is muted (output 0 V voltage), whereas the MOSFET bridge is operated at 5 - kHz switching frequency and 50% duty cycle, suppose to generate square wave excitation voltage. In this operating condition, the frequency-dependent residual effect is negligible. The dc-side voltage is configured to assume different values, which set the peak field strength of the material at 100, 60, and 20 A/m, respectively. The simulated *B–H* characteristic and time-domain primary current as well as secondary voltage waveform are compared to the measurement in Fig. 21(a) and (b). Due to the material nonlinearity together with the coupling of the circuit resistance, the primary current has obvious harmonic component rather than an ideal triangular wave, whereas the secondary voltage is not ideal square wave; all these effects have been well captured by the proposed model. Since the frequency-dependent effect is negligible in this case, so that the per-cycle energy loss is mainly determined by the peak field strength, and the error of the per-cycle energy loss remains approximately the same value as the corresponding cases verified in Section IV (see Fig. 12).

The second scheme imitates the condition where the ferrite material is applied for inductor filter operating in a voltage

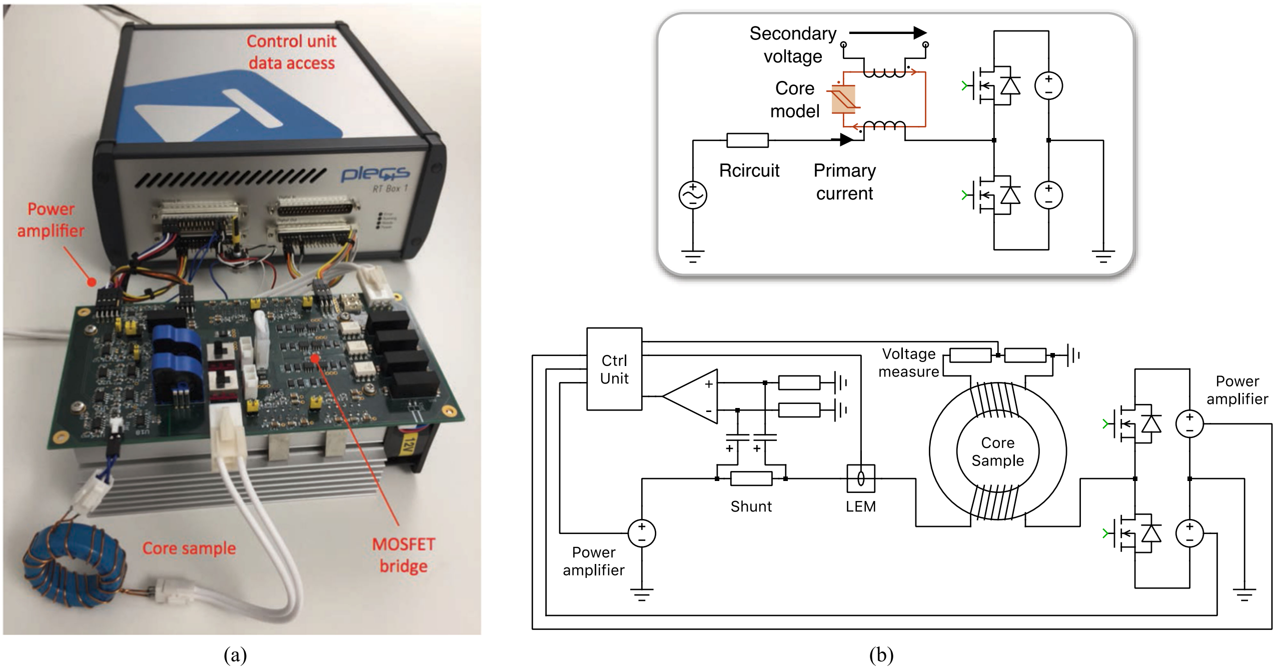

(a) (b)

Fig. 20. (a) Hardware configuration of the test setup with power electronic circuit. (b) Schematic and simulation model of the test setup.

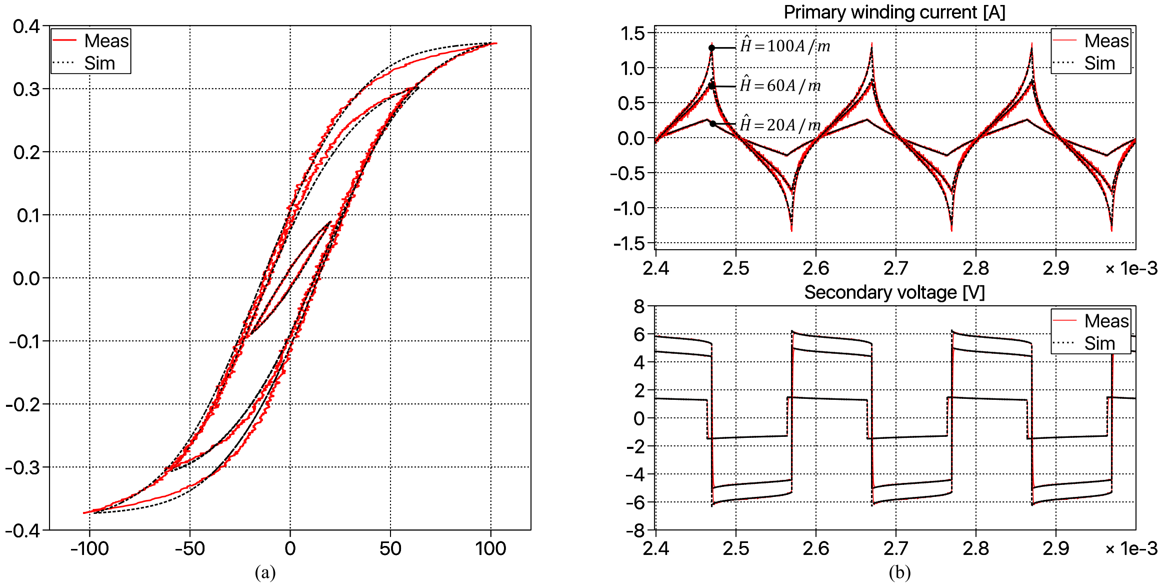

(a) (b)

Fig. 21. Comparison between measurement and simulation of Ferrite N87 in power electronic circuit under 50% PWM modulation. (a) Hysteresis loop. (b) Time-domain primary winding current and secondary voltage.

source inverter. The left-hand-side power amplifier generates 50-Hz sinusoidal voltage and the right-hand-side MOSFET bridge generates pulse width modulation (PWM) voltage. Sinusoidal voltage with 0.24-V amplitude and 50-Hz frequency is generated by the left-hand-side power amplifier. The MOSFET bridge is operated under medium switching frequency 2 kHz with 50% duty cycle and dc voltage of 0.24 V.

The simulated hysteresis loop on the *B*–*H* plane as well as the time-domain primary current and secondary open-circuit voltage are compared in Fig. 22(a) and (b), respectively. The proposed model is able to reproduce the ripple current and pulsed voltage with good accuracy, where the influence of the circuit resistance has been reflected in a fully coupled way. The sinusoidal voltage of the left-hand-side power amplifier contributes to the large hysteresis loop, whereas the right-hand-side MOSFET bridge to the small minor loops. It is to be noted that the minor loops close themselves, which corresponds to the deletion property of the Preisach model as has been discussed in Section II. Both loops have been well captured by the proposed model and the error of energy loss per 50-Hz cycle (including

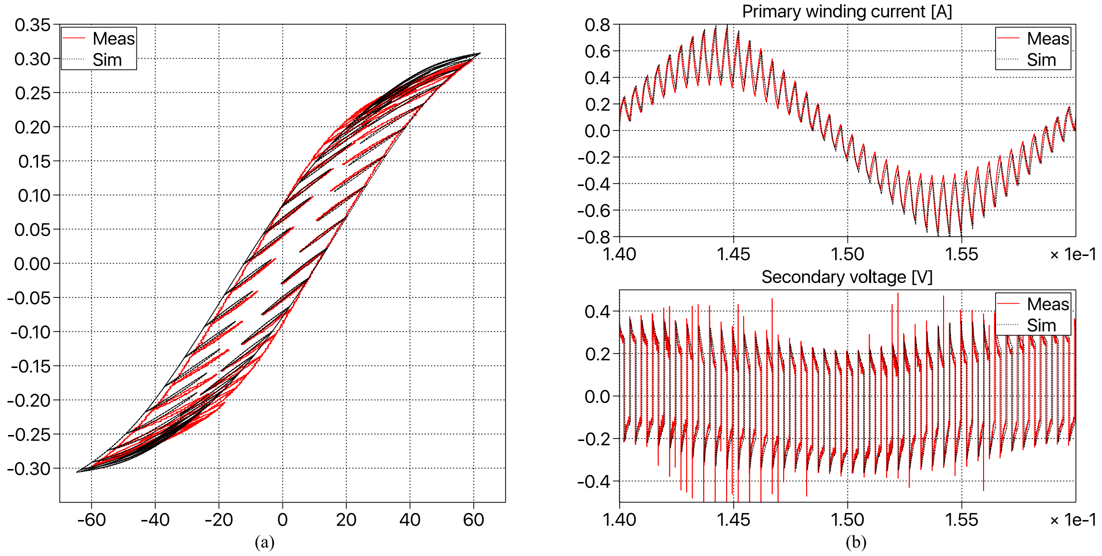

Fig. 22. Comparison between measurement and simulation of Ferrite N87 in power electronic circuit under sinusoidal and 50% PWM modulation. (a) Hysteresis loop. (b) Time-domain primary winding current and secondary voltage.

that from both large major and small minor loops) turns out to be 5%. Please note that there are not only symmetrical but also asymmetrical hysteresis loops present in this verification scheme. The asymmetrical hysteresis loops are not explicitly controlled during the model parameter identification, nevertheless, they are generated by the simulation model as acceptable approximation to the measurement, thanks to the physics-based intrinsic property of the Preisach model.

Finally, it is again to be emphasized that the proposed model only covers frequency-independent hysteresis effect of ferrite materials. If the model is parameterized based on the measurement data obtained at low-frequency sinusoidal excitation (e.g., 200-Hz in this paper), the model should be able to predict the core loss in power electronic converters with limited switching frequency, where the static hysteresis effect dominates. According to the experimental measurements conducted, the per-cycle energy loss of several popular ferrite materials under excitation up to 10 kHz (both sinusoidal and PWM) deviates less than 10% from that obtained under 200 Hz. In this way, the model can be directly applied to high-power applications, such as medium-voltage grid-connected inverters and solid-state transformers, where the switching frequency is usually lower than 10 kHz. For applications with switching frequency above 10 kHz, especially in the case of strongly asymmetrical PWM or with zero-voltage phase (e.g., dual active bridge converter), the frequency-dependent part of core loss becomes observable, including the impact of the duty cycle analyzed by [29] as well as the relaxation effect discussed in [30], which arise from residual mechanisms other than static hysteresis. The frequency-dependent effects require additional resistive components to be included into the magnetic circuit, which is however not in scope of this paper and will be investigated in the future.

VI. CONCLUSION

This work has proposed an improved model for frequency independent hysteresis effect of ferrite materials, using permeance-capacitor analogy based magnetic circuit which can be seamlessly integrated in to system level time domain simulation. Via applying Logistic probability distribution function to the Preisach model of the irreversible magnetisation together with a newly constructed form of B-H function to the reversible magnetisation, the accuracy of the simulated percycle energy loss as well as equivalent permeability of hysteresis loops with wide range of amplitudes can be controlled with good accuracy. The proposed approach of modeling has been verified by ferrite materials of different shapes of hysteresis loop. The fidelity has been evaluated via integrating the model into circuit simulation environment in a fully coupled way. Future work will extend the model to frequency-dependent residual effects and put the accuracy of simulating asymmetrical hysteresis loops also explicitly under control.

REFERENCES

[1] D. Hamill, “Lumped equivalent circuits of magnetic components: The gyrator-capacitor approach,” *IEEE Trans. Power Electron.*, vol. 8, no. 2, pp. 97–103, Apr. 1993.

[2] L. Yan and B. Lehman, “A capacitor modeling method for integrated magnetic components in dc/dc converters,” *IEEE Trans. Power Electron.*, vol. 20, no. 5, pp. 987–995, Sep. 2005.

[3] J. Allmeling, W. Hammer, and J. Schönberger, “Transient simulation of magnetic circuits using the permeance-capacitance analogy,” in *Proc. IEEE 13th Workshop Control Model. Power Electron.*, 2012, pp. 1–6.

[4] M. Luo and D. Dujic, “Permeance based modelling of the core corners considering magnetic material nonlinearity,” in *Proc. Annu. Conf. IEEE Ind. Electron. Soc.*, 2015, pp. 950–955.

[5] M. Luo, D. Dujic, and J. Allmeling, “Leakage flux modeling of multi-winding transformers for system-level simulations,” in *Proc. IEEE Trans. Power Electron.*, vol. 33, no. 3, pp. 2471–2483, Mar. 2018.

[6] I. Mayergoyz, *Mathematical Models of Hysteresis and Their Applications*. New York, NY, USA: Academic, 2003.

[7] F. Liorzou, B. Phelps, and D. L. Atherton, “Macroscopic models of magnetization,” *IEEE Trans. Magn.*, vol. 36, no. 2, Mar. 2000, pp. 418–428.

[8] E. D. Torre, *Magnetic Hysteresis*. Piscataway, NJ, USA: IEEE Press, 1999.

[9] G. Bertotti, F. Fiorillo, and G. P. Soardo, “Dependence of power losses on peak magnetization and magnetization frequency in grain-oriented and non-oriented 3% SiFe,” *IEEE Trans. Magn.*, vol. 23, no. 5, pp. 3520–3522, Sep. 1987.

[10] L.-L. Rouve, T. Waeckerle, and A. Kedous-Lebouc, “Remarks about Preisach function approximation using Lorentzian function and its identification for nonoriented steels,” *IEEE Trans. Magn.*, vol. 31, no. 6, pp. 3557–3559, Nov. 1995.

[11] B. Azzerboni, E. Cardelli, G. Finocchio, and F. L. Foresta, “Remarks about Preisach function approximation using Lorentzian function and its identification for non-oriented steels,” *IEEE Trans. Magn.*, vol. 39, no. 5, pp. 3028–3030, Sep. 2003.

[12] M. Luo, D. Dujic, and J. Allmeling, “Modelling hysteresis of soft core materials using permeance-capacitance analogy for transient circuit simulations,” in *Proc. 19th Eur. Conf. Power Electron. Appl.*, 2017, pp. P.1–P.10.

[13] G. Consolo, G. Finocchio, M. Carpentieri, and B. Azzerboni, “A genetic approach to solve numerical problems in the Preisach model identification,” *IEEE Trans. Magn.*, vol. 42, no. 5, pp. 1526–1537, May 2006.

[14] E. Cardelli, L. Fiorucci, and E. D. Torre, “Identification of the Preisach probability functions for soft magnetic materials,” *IEEE Trans. Magn.*, vol. 37, no. 5, pp. 3366–3369, Sep. 2001.

[15] E. Cardelli, G. Finocchio, and E. Pinzaglia, “Increasing the accuracy of the numerical identification of the modified scalar Preisach model,” *IEEE Trans. Magn.*, vol. 40, no. 2, pp. 892–895, Mar. 2004.

[16] G. Consolo, G. Finocchio, M. Carpentieri, E. Cardelli, and B. Azzerboni, “About identification of scalar Preisach functions of soft magnetic materials,” *IEEE Trans. Magn.*, vol. 42, no. 4, pp. 923–926, Apr. 2006.

[17] D. H. Everett, “A general approach to hysteresis. Part 4—An alternative formulation of the domain model,” *Trans. Faraday Soc.*, vol. 51, pp. 1551–1557, 1955.

[18] R. M. D. Vecchio, “An efficient procedure for modeling complex hysteresis processes in ferromagnetic materials,” *IEEE Trans. Magn.*, vol. 16, no. 5, pp. 809–811, Sep. 1980.

[19] S. R. Naidu, “Simulation of the hysteresis phenomenon using Preisach’s theory,” *IEE Proc.*, vol. 137, no. 2, pp. 73–79, Mar. 1990.

[20] J. G. Zhu, S. Y. R. Hui, and V. S. Ramsden, “A dynamic equivalent circuit model for solid magnetic cores for high switching frequency operations,” *IEEE Trans. Power Electron.*, vol. 10, no. 6, pp. 791–795, Nov. 1995.

[21] S. Y. R. Hui, J. G. Zhu, and V. S. Ramsden, “A generalized dynamic circuit model of magnetic cores for low- and high- frequency applications. II. Circuit model formulation and implementation,” *IEEE Trans. Power Electron.*, vol. 11, no. 2, pp. 251–259, Mar. 1996.

[22] J. T. Hsu and K. D. T. Ngo, “A Hammerstein-based dynamic model for hysteresis phenomenon,” *IEEE Trans. Power Electron.*, vol. 12, no. 3, pp. 406–413, May 1997.

[23] E. D. Torre, J. Oti, and G. Kadar, “Preisach modeling and reversible magnetization,” *IEEE Trans. Magn.*, vol. 26, no. 6, pp. 3052–3058, Nov. 1990.

[24] C. Perez-Rojas, “Fitting saturation and hysteresis via arctangent functions,” *IEEE Power Eng. Rev.*, vol. 20, no. 11, pp. 55–57, Nov. 2000.

[25] D. C. Jiles and D. L. Atherton, “Ferromagnetic hysteresis,” *IEEE Trans. Magn.*, vol. 19, no. 6, pp. 2183–2185, Sep. 1983.

[26] D. C. Jiles, J. B. Thoelke, and M. K. Devine, “Numerial determination of hysteresis parameters for the modeling of magnetic properties using the theory of ferrormangnetic hysteresis,” *IEEE Trans. Magn.*, vol. 28, no. 1, pp. 27–35, Jan. 1992.

[27] E. Cardelli, E. D. Torre, and E. Pinzaglia, “Identifying the Preisach function for soft magnetic materials,” *IEEE Trans. Magn.*, vol. 39, no. 3, pp. 1341–1344, May 2003.

[28] D. Tan, J. L. Vollin, and S. M. Cuk, “A practical approach for magnetic core-loss characterization,” *IEEE Trans. Power Electron.*, vol. 10, no. 2, pp. 124–130, Mar. 1995.

[29] S. Barg, K. Ammous, H. Mejbri, and A. Ammous, “An improved empirical formulation for magnetic core losses estimation under nonsinusoidal induction,” *IEEE Trans. Power Electron.*, vol. 32, no. 3, pp. 2146–2154, Mar. 2017.

[30] J. Muehlethaler, J. Biela, J. W. Kolar, and A. E. Ecklebe, “Improved core-loss calculation for magnetic components employed in power electronic systems,” *IEEE Trans. Power Electron.*, vol. 27, no. 2, pp. 964–973, Feb. 2012.

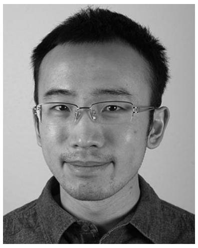

Min Luo (M’13) was born in Beijing, China, in 1986. He received the B.S. degree in electrical engineering from Tsinghua University, Beijing, China, in 2009, and the M.S. degree in electrical power engineering from RWTH Aachen University, Aachen, Germany, in 2012. In 2014, he joined the Power Electronics Laboratory, École Polytechnique Fédérale de Lausanne, Lausanne, Switzerland, as an External Doctoral Research Assistant, where he is currently working toward the Ph.D. degree.

Since 2012, he has been with Plexim as an Application Engineer, working on the software PLECS for fast simulation of power electronic systems. His research interests include dynamic modeling of magnetic components and real-time HIL simulation of power converters.

Drazen Dujic (S’03–M’09–SM’12) received the Dipl.-Ing. and M.Sc. degrees from the University of Novi Sad, Novi Sad, Serbia, in 2002 and 2005, respectively, and the Ph.D. degree from Liverpool John Moores University, Liverpool, U.K., in 2008, all in electrical engineering.

From 2002 to 2006, he was a Research Assistant with the Department of Electrical Engineering, University of Novi Sad, and a Research Associate, from 2006 to 2009, with Liverpool John Moores University. From 2009 to 2013, he was a Principal Scientist with ABB Corporate Research Centre, Zurich, Switzerland, working on the power electronics projects spanning the range from low-voltage/power SMPS in below kilowatt range to medium voltage high-power converters in a megawatt range. During 2010–2011, he was a Member of a project team responsible for the development of the world’s first power electronic traction transformer successfully commissioned on the locomotive. From 2013 to 2014, he was an R&D Platform Manager with ABB Medium Voltage Drives, Turgi, Switzerland, responsible for ABB’s largest IGCT-based medium voltage drive—ACS6000. He is currently an Assistant Professor with the Ecole Polytechnique Federale de Lausanne, Lausanne, Switzerland, and the Director of the Power Electronics Laboratory. He has authored or coauthored more than 80 scientific publications and has filed 11 patents. His research interests include the design and control of advanced high-power electronic systems and high-performance drives.

Prof. Dujic is an Associate Editor for the IEEE TRANSACTIONS ON INDUSTRIAL ELECTRONICS, the IEEE TRANSACTION ON POWER ELECTRONICS, and *IET Electric Power Applications*. He was the recipient of the First Prize Paper Award by the Electric Machines Committee of the IEEE Industrial Electronics Society at IECON-2007, and the Isao Takahashi Power Electronics Award for outstanding achievement in power electronics in 2014.

Jost Allmeling (S’98–M’03) was born in Hamburg, Germany, in 1972. He received the M.S. degree in electrical engineering from Aachen University, Aachen, Germany, in 1996, and the Ph.D. degree from Swiss Federal Institute of Technology (ETH), Zurich, Switzerland, in 2001.

In 1996, he became a Research Associate with the Power Electronics Laboratory, ETH. From 2001 to 2003, he was a Postdoctoral Researcher with the Power Systems Laboratory, ETH. In 2002, he cofounded Plexim, a spin-off company from ETH Zurich that develops the software PLECS for fast simulation of power electronic systems. He is currently the Managing Director of Plexim. His research interests include simulation of power electronics, modeling electrical and mechanical components, real-time HIL simulation, and inverter control.